Commun. Comput. Phys.
doi: 10.4208/cicp.271014.200415a

Vol. **18**, No. 2, pp. 351-379
August 2015

The Diffused Vortex Hydrodynamics Method

Emanuele Rossi[1], Andrea Colagrossi[2,*], Benjamin Bouscasse[2] and Giorgio Graziani[3]

[1] *Department of Mathematics, University of Rome,Sapienza, Rome, 00185, Italy.*
[2] *CNR-INSEAN, Marine Technology Research Institute, Rome, 00128, Italy.*
[3] *Department of Aerospace and Mechanical Engineering, University of Rome, Sapienza, Rome, 00185, Italy.*

Received 27 October 2014; Accepted (in revised version) 20 April 2015

Abstract. A new Particle Vortex Method, called Diffused Vortex Hydrodynamics (DVH), is presented in this paper. The DVH is a meshless method characterized by the use of a regular distribution of points close to a solid surface to perform the vorticity diffusion process in the boundary layer regions. This redistribution avoids excessive clustering or rarefaction of the vortex particles providing robustness and high accuracy to the method. The generation of the regular distribution of points is performed through a packing algorithm which is embedded in the solver. The packing algorithm collocates points regularly around body of arbitrary shape allowing an exact enforcement on the solid surfaces of the no-slip boundary condition. The present method is tested and validated on different problems of increasing complexities up to flows with Reynolds number equal to 100,000 (without using any subgrid-scale turbulence model).

PACS: 47.11.-j, 47.32.C-, 47.54.-r

Key words: Vorticity dynamics, vortex method, particle methods, meshless methods, meshfree methods, packing algorithm, diffused vortex hydrodynamics, body fitted method, vortex wake.

1 Introduction

This work deals with the modelling of viscous incompressible flows using a new particle vortex method called Diffused Vortex Hydrodynamics (DVH).

The use of a vortex method brings several advantages (see *e.g.* [4,9,18]). Firstly, using the vorticity formulation of the Navier-Stokes equation the pressure field is no longer a direct unknown of the problem. The vorticity formulation also allows to discretize with

*Corresponding author. *Email addresses:* e-rossi@mat.uniroma1.it (E. Rossi), andrea.colagrossi@cnr.it (A. Colagrossi), benjamin.bouscasse@cnr.it (B. Bouscasse), g.graziani@uniroma1.it (G. Graziani)

 ©2015 Global-Science Press

https://doi.org/10.4208/cicp.271014.200415a Published online by Cambridge University Press

vortex particles only the rotational region of the flow. Secondly, the boundary conditions at infinity are automatically satisfied, therefore large spatial domains are not required to correctly enforce these boundary conditions. Another advantage is the possibility to move the particles in a Lagrangian way, reducing the numerical dissipation always present with mesh based approach. On the other hand, the pure Lagrangian nature of this method brings also a drawback: a "redistribution techniques" must be introduced in order to preserve the accuracy of the method.

The vortex methods are classified mainly by:

(i) the nature of the discretization used for the vortical region,

(ii) the methods used for the evaluation of the velocity field from the vorticity one,

(iii) the computation of the viscous diffusion process.

The DVH solver presented here is designed to be meshless. As an example of the existing techniques consider the Vortex-in-Cell (ViC) method. In ViC method the velocity field can be solved using highly efficient hybrid particle-mesh algorithms and taking advantage of fast solvers and multigrid methods (see [6]).

Conversely, in DVH the velocity field is obtained using a fast multipole method (FMM), allowing for a complete mesh-free approach for the advection process. The diffusion process does not require a mesh either. A single time step is subdivided into advective and diffusive sub-steps thanks to a splitting algorithm [4]. The diffusion is performed following the deterministic algorithm by Benson et al. [3], by a superposition of elementary solutions of the heat equation. In the present scheme, during diffusion, each vortex particle gives a vorticity contribution on a "Regular Point Distribution" (RPD). This special set of points will then become the new set of vortex particles overwriting the previous one. This procedure prevents the excessive clustering or rarefaction of the vortex particles, and avoids the remeshing procedure which would be required otherwise (see *e.g.* [2]). This problem is common also in the context of other particle methods, for example in the Particle-in-Cell method (the reader can refer to the recent work of *E. Edwards & R. Bridson (2012)* [11]), where the accuracy of the simulations is linked to the interpolation procedure from the particles set to the mesh used for solving the governing equations.

Because there is no any topological connection between the points of the RPDs, the DVH scheme can be considered a pure meshless method.

In the region close to solid bodies, the RPDs are generated using the particle packing algorithm described in [7]. This algorithm is very fast and efficient and, since it is based on particle-dynamic interactions, it can be directly embedded in the same code.

For the regions far from the solid surfaces simple Cartesian lattices, with different sizes according to the distance from the body, can be used as RPDs. In the DVH model, all the different RPDs can overlap each other and can be characterized by different spatial resolutions. Each vortex particle is associated to a RPD at each time step, and during the diffusion each vortex spreads its circulation on the associated RPD.

https://doi.org/10.4208/cicp.271014.200415a Published online by Cambridge University Press

The presence of a solid body within the flow domain results in the introduction of a suitable procedure both to generate vorticity on its surface and to enforce the impermeability constraint. Indeed, the velocity field can be decomposed in the following way $\mathbf{u}=\mathbf{u}_\infty+\mathbf{u}_\omega+\mathbf{u}'$, where $\mathbf{u}_\infty$ is the free stream velocity, $\mathbf{u}_\omega$ is the velocity induced by the vortex particles while $\mathbf{u}'$ is the contribution to the velocity field due to the presence of a body and must be such that it enforces the impermeability condition on the body surfaces while vanishing at infinity. Furthermore, from the value of $\mathbf{u}'$ it is possible to generate the new set of vortices on the body surface enforcing the no-slip condition exactly on its contour (like body fitted methods).

Thus in this work a new Particle Vortex Method is presented and it is used to simulate viscous incompressible flows. The DVH method uses the splitting algorithm of Chorin (1973) [4] to divide the time integration in a sequence of diffusion and advection steps. In the advection step the velocity field is obtained using a convolution sum among the circulations carried by the vortex particles which are then advected by this velocity field. The novelties of the method are in the diffusion step where each vortex particle gives a vorticity contributions on RPDs through the elementary solution of the heat equation. This set of points will then become the new set of vortices substituting the former one. This procedure prevents the excessive clustering or rarefaction of the vortex particles and substitutes remeshing procedures usually adopted in vortex methods. Close to a solid body the RPD is generated through a packing algorithm [7] directly embedded in the code, while far from the body simple Cartesian lattices can be used as RPD. The present method is tested and validated on different problems of increasing complexities up to flows with Reynolds number equal to 100,000 (direct numerical simulation).

The paper is organized as follows: in Section 2 the governing equations are briefly stated. The packing algorithm is recalled in Section 3.1 showing how the different RPDs are generated. In Section 3.2 the procedure for evaluating the velocity field from the vortex particles is described and the boundary condition on the solid surface are commented. In Sections 3.3 and 3.4 the splitting algorithm and the related time step constraints are discussed. In Section 3.5 details on the time integration procedure are given. Finally in Section 4 the DVH model is validated and used on different test cases of increasing complexity.

In the present work the DVH model:

(i) is presented and tested only in a 2D framework,

(ii) body surfaces with singularities are not treated,

(iii) neither moving nor deformable multi bodies are considered,

(iv) subgrid-scale models are not implemented.

In principle the method has not restrictions for tackling the missing topics and those extensions are left for future works.

https://doi.org/10.4208/cicp.271014.200415a Published online by Cambridge University Press

2 Governing equations

Considering a domain Ω the Navier-Stokes equation for a 2D incompressible flow, written in vorticity ω, reads as follows

$$\frac{D\omega}{Dt} = \nu\nabla^2\omega, \qquad \forall \mathbf{r} \in \Omega, \tag{2.1}$$

where t is the time variable, the time derivative is a material derivative and ν is the kinematic viscosity of the considered media. The Navier-Stokes equation simultaneously accounts for the advection and the diffusion of the vorticity field. According to the operator splitting scheme ([4,5]), these two steps can be separately solved in the computational procedure. The numerical solution is therefore obtained by solving an inviscid advection step followed by a purely diffusive one.

In the first step the fluid is considered inviscid and the vorticity is transported according to:

$$\begin{cases} \dfrac{D\omega(\mathbf{r},t)}{Dt} = 0, \\ \dfrac{d\mathbf{r}}{dt} = \mathbf{u}(\mathbf{r},t), \\ \nabla^2\mathbf{u}(\mathbf{r},t) = -\mathrm{curl}(\boldsymbol{\omega}), \quad \boldsymbol{\omega} = \omega\mathbf{e}_3, \end{cases} \tag{2.2}$$

where $\mathbf{r}$ and $\mathbf{u}$ are the position and velocity of a generic material point respectively. These points move following their lagrangian path and conserving their vorticity. To advect numerically the material points a solution of the Poisson equation, which links velocity and vorticity, is needed.

During the diffusive step the fluid is considered at rest and the vorticity diffusion is obtained by solving the linear heat equation:

$$\frac{\partial\omega}{\partial t} = \nu\nabla^2\omega. \tag{2.3}$$

In the DVH scheme this second step is solved by using a deterministic diffusion algorithm described in [3] and briefly recalled in Section 3.4. Further details can also be found in [15].

The presence of a body within the flow field requires to add an appropriate process, between the advection and the diffusion steps, to generate vorticity on the solid walls so to enforce the no slip boundary condition which is discussed in Section 3.2. Concerning the evaluation of the hydrodynamic loads acting on the solid body, the procedure described in [8] is adopted (a deeper theoretical discussion is presented in [13,23]).

2.1 Vortex particle discretization of the vorticity field

In particle vortex methods the vorticity field is discretized in N vortices each with positions $\mathbf{r}_j$ and circulation $\Gamma(\mathbf{r}_j,t)$, denoted for the sake of simplicity as $\Gamma_j(t)$. From the

https://doi.org/10.4208/cicp.271014.200415a Published online by Cambridge University Press

circulation of these particles it is possible to reconstruct the spatial distribution of the vorticity through a mollification procedure:

$$\omega(\mathbf{r},t)=\sum_{j=1}^{N}\Gamma_j(t)\delta_\epsilon(\boldsymbol{r}-\boldsymbol{r}_j), \tag{2.4}$$

where δ_ϵ is a positive smooth approximation of the Dirac δ function such that $\delta_\epsilon\to 0$ as $\epsilon\to 0$ (this function is indicated in the literature as mollifier or kernel function). An example of mollifier function is:

$$\delta_\epsilon(\boldsymbol{r}-\boldsymbol{r}_j):=\frac{1}{\pi(2\epsilon)^2}\exp\left[-\frac{(r-r_j)^2}{(2\epsilon)^2}\right]. \tag{2.5}$$

One of the drawbacks of all the pure Lagrangian vortex methods is that they can lead, during the time evolution, to particle distributions with excessive clustering or rarefaction, and in such condition the vorticity evaluation through Eq. (2.4) can be very poor.

The usual way to restore the consistency of Eq. (2.4) is to introduce procedure to reorganize the vorticity distribution on a regular grid, generating a new set of particles with regular spatial distribution that substitute the former one. The circulation of the new set of particles is given through an opportune interpolating function preserving vorticity momentums up to a desired order. Example of interpolating functions are the M4-kernel, described in [16], (see e.g. [12]) or the Radial Basis Functions (see e.g. [1,2]).

In the DVH the scheme has been simplified avoiding the use of such remeshing procedures using the RPDs during the diffusive step. All the points belonging to the same RPD have a relative distance close to a mean value Δr which characterizes the spatial resolution of the considered RPD. Each particle is associated with a given RPD and gives its vorticity contribution during the diffusive step to these points. At the end of the diffusive step each RPD becomes a new set of vortex particles. Details of this procedure are given in the next section.

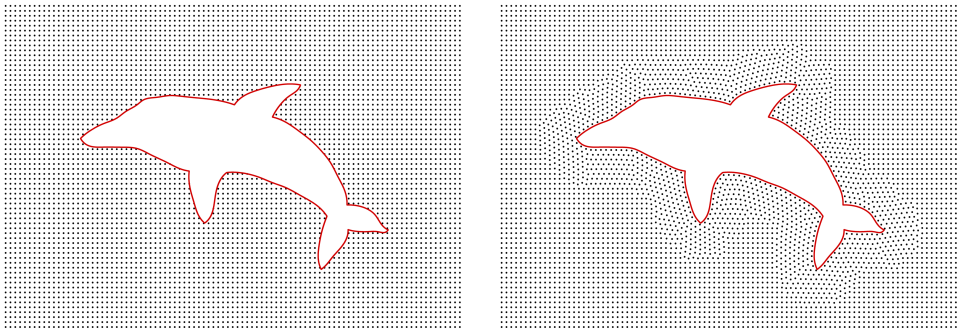
3 DVH scheme details

3.1 RPD generation around body of arbitrary geometry

The RPDs around the body are generated using a packing algorithm described in [7]. This algorithm permits to arrange points around complex contours almost preserving the volume around each point. The computational cost of the packing algorithm is negligible with respect to the cost of the flow simulation. Indeed, the RPDs are generated only before the start of the simulation. Furthermore, this algorithm is based on a simple particle-interactions model, and, therefore, it can be embedded easily in the DVH code.

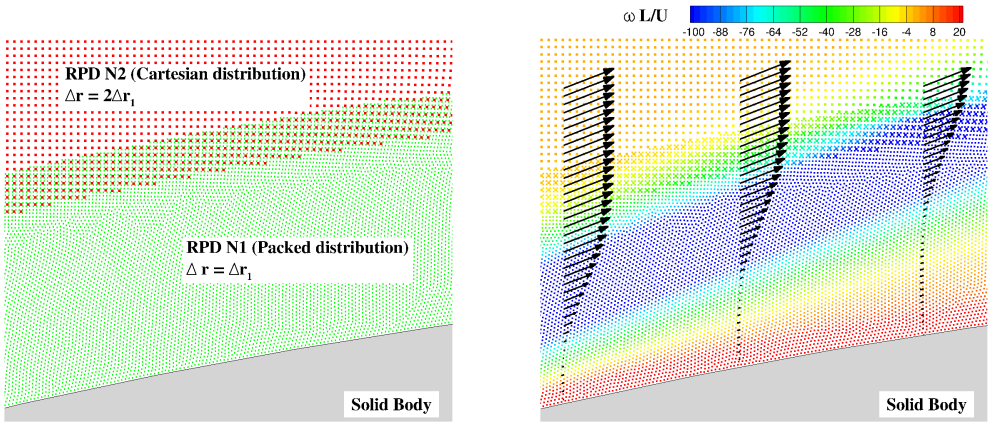
The body contour points are read by the code as an external file, then a spline representation is used in order to change the discretization with a desired spacing Δs. As a second step, points are placed around the body on a regular lattice with spacing Δr (see Fig. 1(a)) then the packing algorithm starts producing the new RPD (see Fig. 1(b)) which

https://doi.org/10.4208/cicp.271014.200415a Published online by Cambridge University Press



(a) (b)

Figure 1: RPD generation around a body of general shape: (a) before packing, (b) after packing.



(a) (b)

Figure 2: Multiple RPDs around a solid surface (enlarged view): (a) Points distribution close and far from the body, (b) vorticity contour and velocity profiles in a region close to a flow separation.

will be used for the viscous diffusion process in the DVH scheme. From Fig. 1(b) it is possible to see that at a certain distance the points are left on the Cartesian lattice.

If the considered body has symmetries, in order to preserve them on the RPD they need to be explicitly enforced. Indeed, the packing algorithm is based on a simplified SPH model, and even if it starts with all the particles arranged in a symmetrical configuration, small asymmetries in the particle positions and velocities develop in time due to errors summation. These small asymmetries can induce wake perturbations and vortex shedding can develop without the necessity of using any perturbation techniques (see Section 4). The same happens in SPH simulation [21]. Both in DVH and SPH the genesis of these flow asymmetries reduces for decreasing Δr.

Once the RPD is generated around the solid body, it is possible to use simple Cartesian distributions far from it. An example is given in Fig. 2(a). There, close to the solid

https://doi.org/10.4208/cicp.271014.200415a Published online by Cambridge University Press

surface a packed configuration is used as a first RPD; far enough from the body a second RPD is used with points set on a Cartesian lattice and using a coarser spatial resolution. Fig. 2(b) shows the vorticity field in the boundary layer region evaluated through Eq. (2.4) and three velocity profiles are computed through a second convolution summation (see Eq. (3.16)). From the results depicted in this figure it can be noticed that the overlapping of the two RPDs does not create problems when convolution summations are used to evaluate vorticity and velocity fields. Considering a body moving with an arbitrary motion, only the closest RPD needs to be moved while the other RDPs, being a simple Cartesian lattice, can be easily updated. The latter situation is not treated in the present work.

3.2 Velocity field evaluation

As already stated in Section 1, the velocity field can be written as a sum of three fundamental contributions

$$\mathbf{u} = \mathbf{u}_\infty + \mathbf{u}_\omega + \mathbf{u}', \tag{3.1}$$

where $\mathbf{u}_\infty$ is the free stream velocity, $\mathbf{u}_\omega$ is the velocity contribution due to the vorticity field itself and, finally, $\mathbf{u}'$ is the velocity field contribution which allows for the enforcement of the impermeability condition on the solid surfaces.

The contribution $\mathbf{u}_\omega$ and can be expressed as (here and in what follows the integrated variable will be denoted with a superscript *):

$$\begin{cases} \mathbf{u}_\omega(\mathbf{r}) = \displaystyle\int_\Omega \mathbf{K}(\mathbf{r},\mathbf{r}^\star)\omega(\mathbf{r}^\star)dS^\star, \\ \mathbf{K}(\mathbf{r},\mathbf{r}^\star) := \nabla^\perp G(\mathbf{r},\mathbf{r}^\star) = -\dfrac{1}{2\pi}\mathbf{e}_3 \times \dfrac{(\mathbf{r}-\mathbf{r}^\star)}{|\mathbf{r}-\mathbf{r}^\star|^2}, \end{cases} \tag{3.2}$$

where $\nabla^\perp$ indicates the skew gradient operator, G is the free space Green function of the Laplace equation, in a 2D framework:

$$G(\mathbf{r},\mathbf{r}^\star) = -1/(2\pi)\ln|\mathbf{r}-\mathbf{r}^\star|$$

and $\mathbf{e}_3$ the normal unit vector orthogonal to the fluid domain plain. Eq. (3.2) represents the solution of the Poisson equation (2.2) for an infinite fluid domain, *i.e.* in the absence of boundaries.

The velocity due to the vortex particles at a generic point $\mathbf{r}$ can be expressed by discretizing Eq. (3.2) as:

$$\mathbf{u}_\omega(\mathbf{r},t) = \sum_{j=1}^{N} \Gamma_j(t)\mathbf{K}_\epsilon(\mathbf{r},\mathbf{r}_j), \tag{3.3}$$

where $\mathbf{K}_\epsilon$ is a mollified version of the kernel $\mathbf{K}$ (see e.g. [15]) and N is the total number of vortex particles.

Using directly Eq. (3.3) to compute the velocity would have a CPU cost of order N^2. In order to speed-up the Biot-Savart velocity summation a Barnes-Hut method with a

https://doi.org/10.4208/cicp.271014.200415a Published online by Cambridge University Press

multipole expansion is adopted reducing the computational cost to order $N\log N$ (see [14,27] for more details).

3.2.1 Enforcement of the boundary conditions on the body surface

In order to satisfy the boundary conditions on the body surface, the contribution $\mathbf{u}'$ is necessary. Using an indirect integral representation of the velocity field, $\mathbf{u}'$ can be written as:

$$\mathbf{u}'(\mathbf{r}) = -\int_{\partial\Omega_{body}} \sigma(\mathbf{r}^\star)\nabla G(\mathbf{r},\mathbf{r}^\star)d\mathbf{r}^\star + \int_{\partial\Omega_{body}} \gamma(\mathbf{r}^\star)\nabla^\perp G(\mathbf{r},\mathbf{r}^\star)d\mathbf{r}^\star, \tag{3.4}$$

where the body contribution to the velocity field is described in terms of sources $\sigma(\mathbf{r})$ and circulation $\gamma(\mathbf{r})$ distributions. We now introduce a formulation of $\mathbf{u}'$ in terms of complex variables [14]. Defining the complex velocity:

$$q(z) := u_x(x,y) - iu_y(x,y), \tag{3.5}$$

being u_x and u_y the two velocity components, the hybrid integral representation of the velocity field for Eq. (3.4) reads

$$\begin{cases} f(z) := \dfrac{i\sigma(z)+\gamma(z)}{\tau(z)}, \qquad \mathcal{K}(z,z^\star) := \dfrac{1}{z-z^\star}, \\ q'(z) = \dfrac{1}{2\pi i}\displaystyle\int_{\partial\Omega_{body}} f(z^\star)\mathcal{K}(z,z^\star)dz^\star, \quad \forall z\in\Omega, \\ q'(z) = \dfrac{1}{2}f(z) + \dfrac{1}{2\pi i}\displaystyle\oint_{\partial\Omega_{body}} f(z^\star)\mathcal{K}(z,z^\star)dz^\star, \quad \forall z\in\partial\Omega_{body}, \end{cases} \tag{3.6}$$

where $\tau = \tau_x + i\tau_y$ is the complex tangent to the body contour. The second and third equations of (3.6) give respectively the contribution to the velocity field in a generic point of the fluid domain as well as on the points laying on the body contour, due to the presence of the body.

The body surface is discretized in N_b elements of equal length Δs and a curvilinear abscissa s is considered when moving along this surface. The last equation of system (3.6) can be discretized using a quadrature rule and the velocity $\mathbf{u}'$ on the body surface can be written in complex variable as:

$$\begin{aligned} q'(z_k) = -\frac{1}{2\pi i}\left[f(z_k)\tau(z_k)\overline{\frac{d^2z}{ds^2}(z_k)} + \frac{1}{\tau(z_k)}\left(i\frac{d\sigma}{ds}(z_k) + \frac{d\gamma}{ds}(z_k)\right)\right] \\ + \frac{1}{2}f(z_k) + \frac{1}{2\pi i}\sum_{j=1}^{N_b}\left[\frac{i\sigma(z_j)+\gamma(z_j)}{z_k-z_j}\right]\Delta s, \qquad z_k, z_j \in \partial\Omega_{body} \end{aligned} \tag{3.7}$$

being the indices k, j the generic k-th and j-th elements on the body surface.

In Eq. (3.7) the distribution of circulation γ is also unknown, however, a constant distribution for γ can be considered and the value can be set using the Kelvin theorem:

$$\gamma(z_k) = \frac{\Gamma(t_0)-\Gamma(t)}{\mathcal{P}} \qquad \forall k\in[1,N_b], \tag{3.8}$$

https://doi.org/10.4208/cicp.271014.200415a Published online by Cambridge University Press

where $\Gamma(t_0)$ is the circulation around the body at initial time t_0, $\Gamma(t)$ is the circulation evaluated as the sum of the circulations of all the vortex particles in the fluid domain, *i.e.*:

$$\Gamma(t)=\sum_{j=1}^{N}\Gamma_j \tag{3.9}$$

and $\mathcal{P}$ is the perimeter of the body. By using constant γ along the body contour its derivative disappears in Eq. (3.7). Note that Eq. (3.9) holds if the computational domain is large enough to enclose all the vortex particles, otherwise the circulation around the boundary of the fluid domain should be kept into account in order to correctly evaluate the circulation around the body.

If we multiply Eq. (3.7) by τ, taking the real and the imaginary parts of the equation, the normal, $u_n=\mathbf{u}\cdot\mathbf{n}$, and tangent, $u_\tau=\mathbf{u}\cdot\boldsymbol{\tau}$, velocity components on the body contour can be expressed. Rearranging the two discretized equations in a matrix formalism, we get:

$$\begin{cases} \{u_n\}=-\left[\dfrac{1}{2}\mathbb{I}+\Delta s\,\mathfrak{I}(\mathbb{F})\right]\{\sigma\}+[\Delta s\,\mathfrak{R}(\mathbb{F})]\{\gamma\}, \\ \{u_\tau\}=\left[\dfrac{1}{2}\mathbb{I}+\Delta s\,\mathfrak{I}(\mathbb{F})\right]\{\gamma\}+[\Delta s\,\mathfrak{R}(\mathbb{F})]\{\sigma\}-\dfrac{\Delta s}{2\pi}\left\{\dfrac{d\sigma}{ds}\right\}, \end{cases} \tag{3.10}$$

being $\{\cdot\}$ the array containing all the values of a generic quantity on the N_b body elements while the complex matrix $\mathbb{F}=\mathfrak{R}(\mathbb{F})+i\mathfrak{I}(\mathbb{F})$ is:

$$\mathbb{F}_{k,j}:=-\frac{1}{2\pi}\begin{cases} \dfrac{\tau}{(z_j-z_k)}, & k\neq j, \\ \overline{\left(\dfrac{d^2z}{ds^2}\Big/2\dfrac{dz}{ds}\right)}, & k=j. \end{cases} \tag{3.11}$$

The impermeability condition can be enforced on all the N_b body elements through the first equation of (3.10):

$$\left[\frac{1}{2}\mathbb{I}+\mathfrak{I}(\mathbb{F})\Delta s\right]\{\sigma\}=-\{\mathbf{u}_{body}\cdot\mathbf{n}\}+\{\mathbf{u}_\infty\cdot\mathbf{n}\}+\{\mathbf{u}_\omega\cdot\mathbf{n}\}+[\mathfrak{R}(\mathbb{F})\Delta s]\{\gamma\}, \tag{3.12}$$

being $\{\mathbf{u}_{body}\}$ the prescribed velocity of the N_b elements of the body. Through the linear system (3.12), knowing the values of the arrays $\{\mathbf{u}_{body}\}$, $\{\mathbf{u}_\infty\}$ and $\{\mathbf{u}_\omega\}$, the strength of the sources $\{\sigma\}$ can be evaluated.

Once the $\{\sigma\}$ distribution is calculated, the tangential velocity field on the body can be obtained by means of the second equation of (3.10):

$$\{u_\tau\}=\left[\frac{1}{2}\mathbb{I}+\mathfrak{I}(\mathbb{F})\Delta s\right]\{\gamma\}+[\mathfrak{R}(\mathbb{F})\Delta s]\{\sigma\}-\frac{\Delta s}{2\pi}\left\{\frac{d\sigma}{ds}\right\}+-\{\mathbf{u}_{body}\cdot\tau\}+\{\mathbf{u}_\infty\cdot\tau\}+\{\mathbf{u}_\omega\cdot\tau\}. \tag{3.13}$$

https://doi.org/10.4208/cicp.271014.200415a Published online by Cambridge University Press

Finally, the no slip boundary condition can be enforced by generating a new set of vortices on the body contour with the circulation of each vortex defined as:

$$\Gamma_k^{new} := u_\tau(\mathbf{r}_k)\Delta s, k \in [1, N_b]. \tag{3.14}$$

This new set of vortices is now free to diffuse and move, together with the other vortices already present in the computational domain, according to Eqs. (2.2) and (2.3).

After the diffusion of the new vortices on the boundary, it is necessary to evaluate $\gamma(z_k)$ according to Eq. (3.8).

3.2.2 Body contribution to the velocity field

Knowing the (discrete) distribution of sources and vortices on the body surface, we can compute the contribution to the velocity field due to the presence of the body for a generic point $\mathbf{r}$ in the domain. The advantage of using the integral representation (3.4) is that $\mathbf{u}'$ can be evaluated by means of the same representation adopted for $\mathbf{u}_\omega$ (see *e.g.* [14]):

$$\mathbf{u}'(\mathbf{r},t) = \sum_{k=1}^{N_{body}} [\mathbf{K}_\epsilon(\mathbf{r},\mathbf{r}_k)\gamma_k(t) - \mathbf{e}_3 \times \mathbf{K}_\epsilon(\mathbf{r},\mathbf{r}_k)\sigma_k(t)]\Delta s, \tag{3.15}$$

where $\mathbf{r}_k$ is the position of the k-th generic body element and Δs is the corresponding length. Therefore $(\{\sigma\},\{\gamma\})$ distributions can be added to the vortex particle array before calling the subroutines for the Barnes-Hut and for the multipole procedures.

3.3 Advection step

Putting together Eqs. (3.1), (3.3) and (3.15) the velocity can be evaluated on the whole set of vortex particles, then each vortex can be displaced accordingly carrying its own circulation:

$$\begin{cases} \dfrac{D\Gamma_i(t)}{Dt} = 0, \\ \dfrac{d\mathbf{r}_i(t)}{dt} = \mathbf{u}(\mathbf{r}_i,t), \\ \mathbf{u}(\mathbf{r}_i,t) = \mathbf{u}_\infty + \displaystyle\sum_{j=1}^{N_{vortex}} \Gamma_j(t)\mathbf{K}_\epsilon(\mathbf{r}_i,\mathbf{r}_j) + \sum_{k=1}^{N_{body}} [\mathbf{K}_\epsilon(\mathbf{r}_i,\mathbf{r}_k)\gamma_k(t) - \mathbf{e}_3 \times \mathbf{K}_\epsilon(\mathbf{r}_i,\mathbf{r}_k)\sigma_k(t)]\Delta s. \end{cases} \tag{3.16}$$

The numerical time integration is performed through a fourth order Runge-Kutta algorithm using a specific time step, Δt_a, for all the vortex particles (see Section 3.5).

3.4 Diffusion step

3.4.1 Diffusion of a single vortex particle in free-space

Viscous effects are accounted for in the diffusive step where the fluid velocity is neglected and the diffusion of the field vortices is evaluated by solving Eq. (2.3). Thanks to the

https://doi.org/10.4208/cicp.271014.200415a Published online by Cambridge University Press

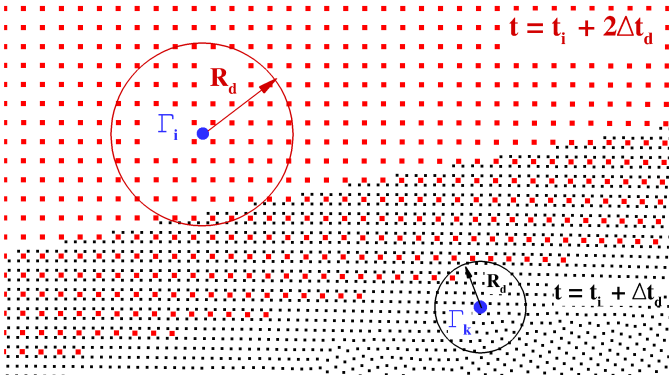


Figure 3: Sketch of the vorticity diffusion of two vortex particles in free space using the two associated RPDs.

linearity of this equation, the solution can be approximated as a sum of elementary solutions. For a single vortex particle with position $\mathbf{r}_i$ and strength Γ_i, the analytical solution of the heat equation can be expressed at time $t=t_0+\Delta t_d$ as:

$$\begin{cases} \omega(\mathbf{r},t_0+\Delta t_d)=\Gamma_i\dfrac{1}{4\pi\nu\Delta t_d}\exp\left[-\dfrac{(r-r_i)^2}{4\nu\Delta t_d}\right], & \text{if } |\mathbf{r}-\mathbf{r}_i|\le R_d, \\ \omega(\mathbf{r},t_0+\Delta t_d)=0, & \text{otherwise,} \end{cases} \tag{3.17}$$

where the gaussian distribution has been truncated at distance R_d for numerical purpose. R_d is called "diffusive radius" and it is a key parameter of the convergence properties of the DVH scheme (see [24]). The relative error in the conservation of circulation introduced by this truncation is:

$$\xi=\left|\frac{\Gamma(t_0+\Delta t_d)-\Gamma(t_0)}{\Gamma(t_0)}\right|=\exp\left(-\frac{R_d^2}{4\nu\Delta t_d}\right). \tag{3.18}$$

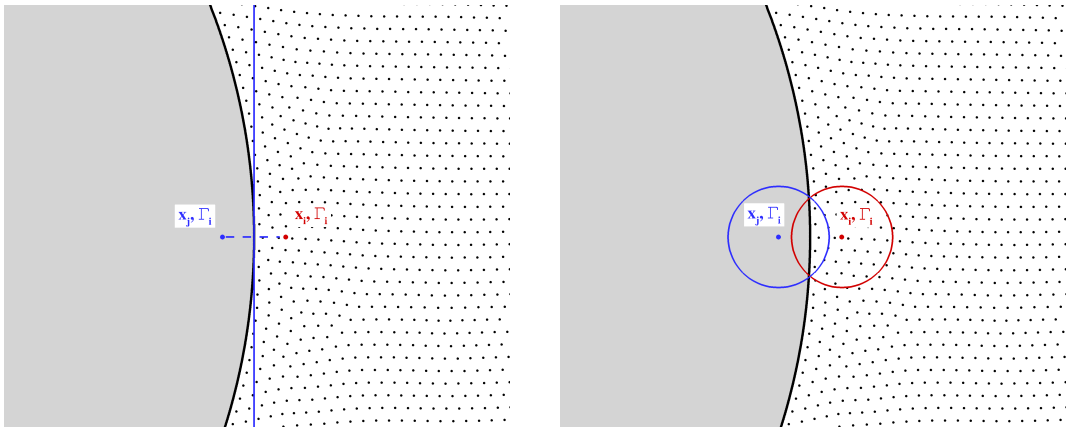
This expression is used in the next section to determine the diffusive time step Δt_d.

Following [3], Eq. (3.17) can be used to distribute the vorticity of each vortex over its associated RPD which is characterized by a resolution length Δr (see sketch in Fig. 3). A renormalization procedure is used to preserve the conservation of the circulation given by each vortex to the RPD (see [24]). In this way the DVH scheme preserves the total circulation as requested by the Kelvin's circulation theorem.

3.4.2 Diffusion in the presence of a solid boundary

Difficulties in treating solid boundary condition when using particle methods are quite common and usually a ghost-fluid approach is used to tackle this problem (see *e.g.* [20, 25]). For the present DVH scheme, if the vortex particle is at a distance from a solid surface that is less than R_d, the presence of this boundary needs to be taken into account in the solution of the heat equation. A vanishing normal derivative of the vorticity is

https://doi.org/10.4208/cicp.271014.200415a Published online by Cambridge University Press



(a) (b)

Figure 4: Diffusion in the presence of a solid boundary: (a) construction of the image vortex, (b) points of the RPD influenced by diffusion.

enforced at the boundary, hence, a simple reflection condition on the diffusion of the vorticity near the boundary is considered in this step.

If the diffusive radius R_d is small enough to make the body curvature not relevant, it is possible to locally approximate the body with a straight line. In this case the diffusion near the body can be solved using the method of image vortices: for every vortex an image vortex inside the body is created symmetrically along the direction of the local normal. The contribution to the vortex diffusion is now taken into account by diffusing the image vortex hence reflecting inside the domain the otherwise outgoing vorticity.

This technique can be generalized in the presence of geometrical singularity using an algorithm to account for each vortex close to body vertex, however, in the present paper this aspect is not further developed and it is left for future works.

3.5 Choice of time steps

Considering U and L as the reference velocity and length of the problem, the Reynolds number is defined as $\mathrm{Re}=UL/\nu$.

In the test cases of Section 4 the characteristic velocity used for the definition of the Reynolds number is the modulus of the free stream velocity $U=|\mathbf{u}_\infty|$. The characteristic length used is the diameter D for the simulation of the cylinder and the C-shape body wakes, the chord c for the simulations of the ellipse and airfoil wakes.

For the sake of simplicity a single RPD is considered with the linked spatial resolution equal to $L/\Delta r$.

Using Eq. (3.18) it is possible to define the diffusive time step in the following way

$$\Delta t_d \frac{U}{L} = \frac{(R_d/\Delta r)^2}{4\ln(1/\xi)} \frac{1}{(L/\Delta r)^2} \mathrm{Re}, \tag{3.19}$$

https://doi.org/10.4208/cicp.271014.200415a Published online by Cambridge University Press

Eq. (3.19) allows for the evaluation of the diffusion time step from the spatial resolution $L/\Delta r$, the ratio $R_d/\Delta r$ and the Reynolds number, once the error ξ has been fixed. The parameters used in this work are: $\xi = 10^{-5}$, $R_d/\Delta r = 4$ and therefore the expression (3.19) can be rewritten as:

$$\Delta t_d \frac{U}{L} \simeq 0.34 \frac{\mathrm{Re}}{(L/\Delta r)^2}. \tag{3.20}$$

The advection time step Δt_a can be chosen by considering the flow velocity U and the discretization Δr used during the diffusion step. A first evaluation of Δt_a can be chosen as:

$$\Delta t_a \frac{U}{L} = \mathrm{Co} \frac{1}{(L/\Delta r)}, \tag{3.21}$$

where Co is the Courant number. In the present work Co is maintained close to 1 to avoid that the vortex particles move with large displacements inducing particle disorder during the advective steps. Indeed, for the Reynolds number analysed in this work and for the ratios $L/\Delta r$ possible with the CPU resource available, this second constraint is always less restrictive than that related to the diffusion process (*i.e.* $\Delta t_a < \Delta t_d$, this inequality reverses when considering highly viscous flow or very high spatial resolutions).

This means that during a time interval Δt_d more than one advection step can be performed. In order to synchronize diffusion and advection steps, once Δt_a has been evaluated, it has to be rearranged to get Δt_d and Δt_a in an integer ratio:

$$N_{\Delta t} = \left[\frac{\Delta t_d}{\Delta t_a} \right] \rightarrow \Delta t_a = \frac{\Delta t_d}{N_{\Delta t}}, \tag{3.22}$$

resulting in a correction to the real Courant number used in the simulations with respect to that initially imposed (for more details see also [24]).

To contain the growth of the number of vortex particles during the diffusion step, different RPDs with decreasing resolutions are adopted for increasing distance from the body. It means that vortex particles are characterized by different diffusion time steps while all of them are moved with the same Δt_a. To synchronize the diffusion process the Δt_d for each RPDs must be chosen such that they are in integer ratio with each other (see sketch of Fig. 3).

4 Numerical results

In this section the DVH model is tested by studying flows past solid bodies of various shapes at different Reynolds numbers.

The simulations are performed using a multi resolution approach: the spatial resolution is decreased for increasing distance from the body in the flow direction, in particular this is done using several RPDs with decreasing values of $L/\Delta r$ as shown in Fig. 5. The first RPD (*i.e.* the one nearest to the body) is generated using the procedure described in Section 3.1.

https://doi.org/10.4208/cicp.271014.200415a Published online by Cambridge University Press

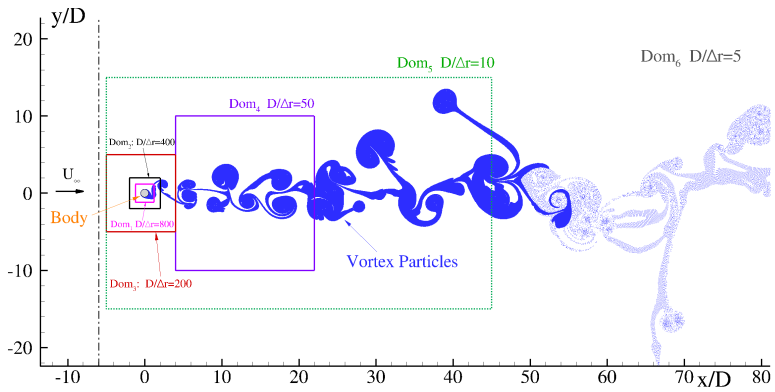


Figure 5: Example of a multi-domain simulation using 6 different RPDs.

A first series of simulation is made (Section 4.1) to study the flow past a thick elliptical cylinder at Re= 500, in this case a convergence test is shown. The DVH solution is then compared with another particle method, the Smoothed Particle Hydrodynamics (SPH), using the numerical model described in [21] and in [19].

In Section 4.2 the flow past a thin ellipse with angle of attack $\alpha = 30°$ at Re= 3000 is simulated and the results are compared against those presented in the literature (see [17, 22]).

Because the present DVH method is able to perform simulations using bodies of general shape, the flow past a body having a C-shape form is simulated at Re= 2000 for various angles of attack, the results are shown in Section 4.3.

In Section 4.4 the flow past a circular cylinder is simulated for Re= 9500, the obtained results are compared with the available data (see [18]).

In the last section (Section 4.5) the flow past a circular cylinder is simulated for Reynolds numbers equal to 5×10^4 and 10^5. This last simulation requires a very high spatial resolution in the boundary layer region, for this purpose eight RPDs are used. Even if this is a 2D simulation, for our knowledge is, at the time of writing, the flow around a circular cylinder with highest Reynolds number simulated in the literature without using any subgrid-scale turbulence model.

The simulations performed in this work are 2D-DNS since no averaging or filtering subgrid-scale model have been adopted. To correctly use a DNS technique all the vorticity scales need to be reproduced, hence, the local Reynolds number $\mathrm{Re}_{\Delta r} = U\Delta r/\nu$ must be of order one, meaning that the Kolmogorov scale is correctly resolved. This constrain on $\mathrm{Re}_{\Delta r}$, for a given Reynolds number, limits the range of spatial resolutions usable, at least for the domain closest to the body.

4.1 Inclined elliptical cylinder Re = 500

A series of simulations of an elliptical cylinder with axis ratio 0.4 and angle of attack $\alpha = 20°$ is performed at Re= 500. An example of the evolution of the vorticity profile is

https://doi.org/10.4208/cicp.271014.200415a Published online by Cambridge University Press

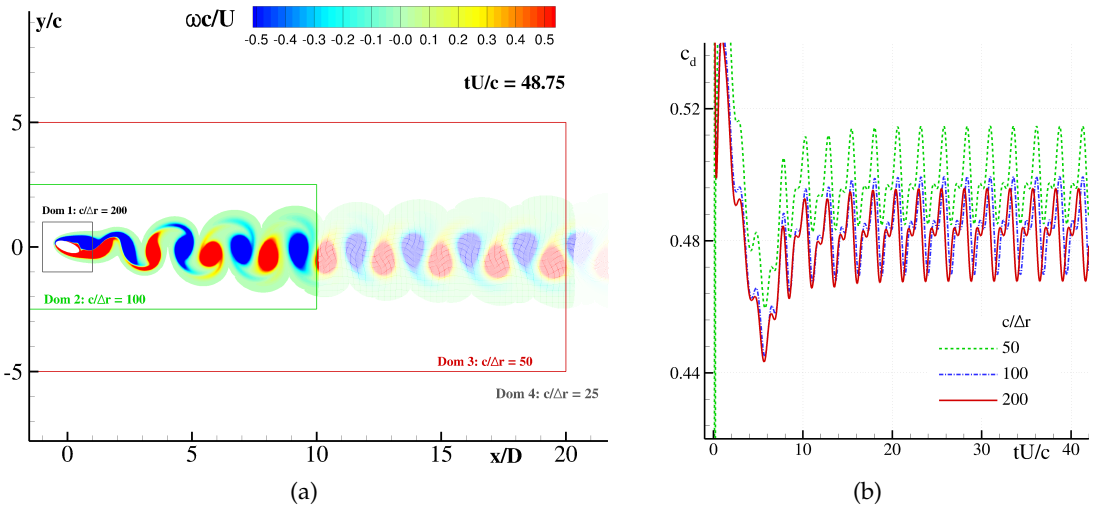


Figure 6: (a) Evolution of the vorticity field for $c/\Delta r = 200$ for an elliptical cylinder (axis ratio 0.4, $\alpha = 20°$) at Re=500, (b) drag coefficient for three different spatial resolutions $c/\Delta r$.

shown in Fig. 6(a) for $c/\Delta r = 200$ (being c the major axis). At this Reynolds and for the adopted thickness a regular harmonic shedding is reached after the transitory stage.

Fig. 6(b) shows the time histories for the drag coefficient c_d using three different spatial resolutions $c/\Delta r$ = 50, 100, 200. Table 1 reports for each value of $c/\Delta r$: (i) the cell-Reynolds number $\mathrm{Re}_{\Delta r} = U\Delta r/\nu$, (ii) the Courant number Co used for the advection time step. The low $\mathrm{Re}_{\Delta r}$ values reached with the adopted resolution justify the good accuracy of the simulations performed in this first test-case.

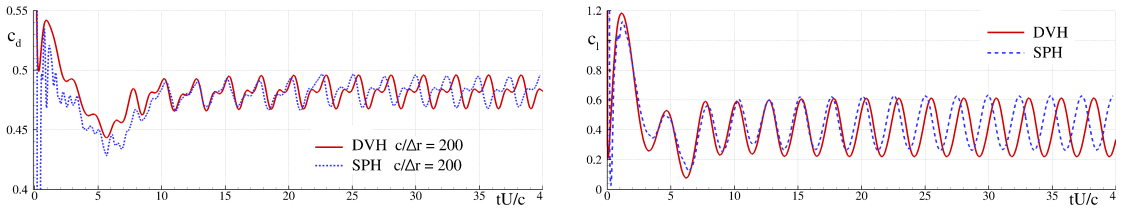
Table 1: Inclined elliptical cylinder Re=500: main discretization parameters.

$c/\Delta r$	$\mathrm{Re}_{\Delta r}$	Co	$\Delta t_a U/c$	$\Delta t_d U/c$ (Dom 1)
50	10	0.88	1.76×10^{-2}	7.05×10^{-2}
100	5	0.88	8.81×10^{-3}	1.76×10^{-2}
200	2.5	0.44	2.20×10^{-3}	4.41×10^{-2}

The convergence ratio calculated, using a L_1 norm in time, is of about 2.0 in agreement with the analysis performed in [24].

The same case is simulated with a Smoothed Particle Hydrodynamics method [21]. Figs. 7(a) and 7(b) depict respectively the drag and lift coefficient obtained with both methods with a spatial resolution $c/\Delta r$=200. A good agreement between the two methods is obtained in the periodic regime. The differences on the transitory stage are mainly due to the weakly compressible approach of the SPH model where an impulsive start of the body originates a series of acoustic waves travelling and reflecting in the domain. The plot 7(b) shows that the lift coefficient oscillates around a positive value, as expected because of the small positive angle of incidence. The Strouhal number $St = Lf/\nu$, being f

https://doi.org/10.4208/cicp.271014.200415a Published online by Cambridge University Press



(a) (b)

Figure 7: Time behaviour of drag (a) and lift (b) coefficient respectively for an elliptical cylinder (axis ratio 0.4, $\alpha = 20^\circ$) at Re=500: comparison between SPH and DVH.

the oscillation frequency, evaluated by the two different solvers is slightly different: the value obtained by DVH is $St = 0.39$ while that evaluated with SPH is $St = 0.41$. This can be related to the confined domain used in the SPH simulation. Difference in the lift and drag coefficients due to confinement are also reported in the experiments of [10] while the difference in the Strouhal number for SPH, with respect to experimental data are shown in [21].

4.2 Flow past an elliptic cylinder at Re = 3000

Following the work of Nair & Sengupta (1997) a DVH simulation of the flow around a thin elliptical cylinder (thickness to chord ratio 0.1) with angle of attack $\alpha = 30^\circ$ is here discussed. The same test case has been performed more recently by Huang & Huang (2013) [17] and therefore also the related data are used to cross validate the DVH model.

In Table 2 the main parameters of the spatial/time resolution adopted are shown. The ratio $c/\Delta r$ used close to the body is 800 allowing for an accurate solution of the boundary layer region.

Table 2: Flow around an elliptic cylinder at Re=3000: main discretization parameters.

$c/\Delta r$	$\mathrm{Re}_{\Delta r}$	Co	$\Delta t_a U/c$	$\Delta t_d U/c$ (Dom 1)
800	3.75	1.32	1.65×10^{-3}	3.52×10^{-3}

Fig. 8 depicts the vorticity field in the near (left) and far (right) regions. The angle of attack used and the small thickness of the body induce a stall regime leading to a very complex wake dynamics.

Fig. 9 reports the pressure coefficient around the ellipse for three different time instants. The pressure profiles have been compared with those evaluated in [22] showing a good agreement with the data produced by the DVH model.

A comparison for the drag and lift coefficients with the results reported in [22] and in [17] is depicted in Fig. 10. Both c_d and c_l coefficient oscillate around the same range of values for all the three sets of data, however the complexity of the vorticity field this time makes impossible to get a fair agreement between the different solutions.

https://doi.org/10.4208/cicp.271014.200415a Published online by Cambridge University Press

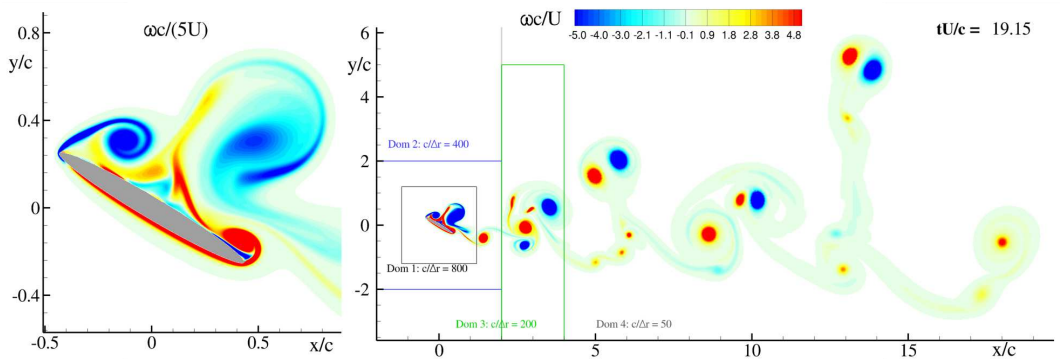
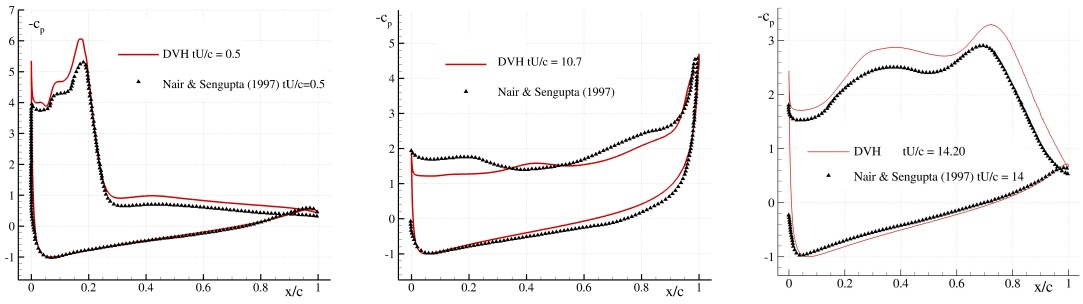
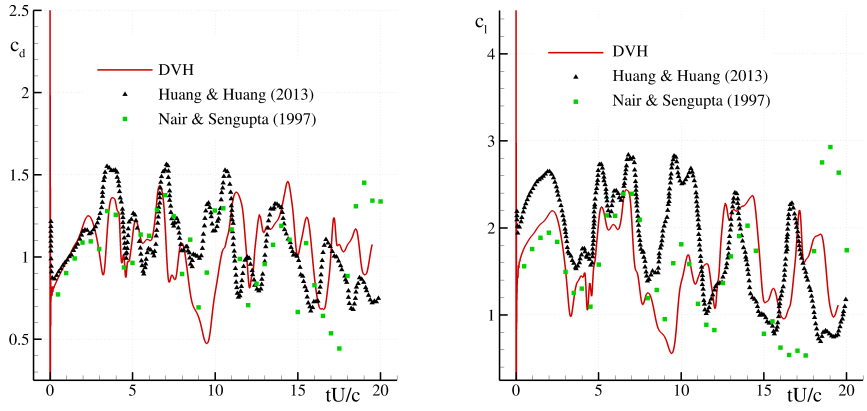


Figure 8: Evolution of the vorticity field for $c/\Delta r = 800$ for an elliptical cylinder (axis ratio 0.1, $\alpha = 30^{\circ}$) at Re=3000. Left: enlarged view close to the body. Right: wake field with the different domains used.



(a) (b) (c)

Figure 9: Pressure coefficients for a thin ellipse at Re=3000 at different times: comparison between Nair & Sengupta (1997) [22] and present study.



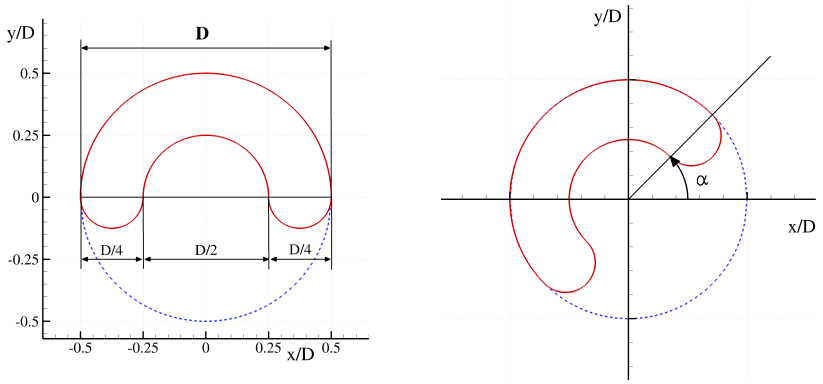
(a) (b)

Figure 10: (a) (b) Drag and lift coefficients respectively for a thin ellipse at Re=3000: comparison between Nair & Sengupta 1997 [22], Huang & Huang 2013 [17] and present study.

https://doi.org/10.4208/cicp.271014.200415a Published online by Cambridge University Press

4.3 Flow around a C-Shape body at Re=2000

The DVH method, thanks to the packing algorithm used to generate the RPDs, allows simulating the viscous flow around body of general shapes. As an example, the flow around a smooth body composed by four semicircles with different radius (Fig. 11(a)) is here analysed. Different orientation changing the angles of attack α (Fig. 11(b)) are also considered.



(a) (b)

Figure 11: (a) Sketch of the C-shape body. (b) Notation for the different rotations considered.

The Reynolds number assumed for this test-case is Re=2000, while the angles of attack used are α=−90°, −45°, 0°, 45°, 90°. Figs. 12(a) and 12(b) show the time records for the drag and lift coefficients respectively for the first three angles $\alpha=-90°$, −45°, 0. For $\alpha=0°$ the force reaches a periodic behaviour after the transition stage. Decreasing α the periodicity is lost and a quite irregular time behaviour develops, furthermore the level of the mean drag largely increases. The lift coefficient has a negative mean for $\alpha=0°$, a positive mean value for $\alpha=-45°$ and a zero mean value for $\alpha=-90°$ as expected. The amplitude of the fluctuation on the lift force at α=−90° is comparable to that recorded for a circular cylinder at the same Re.

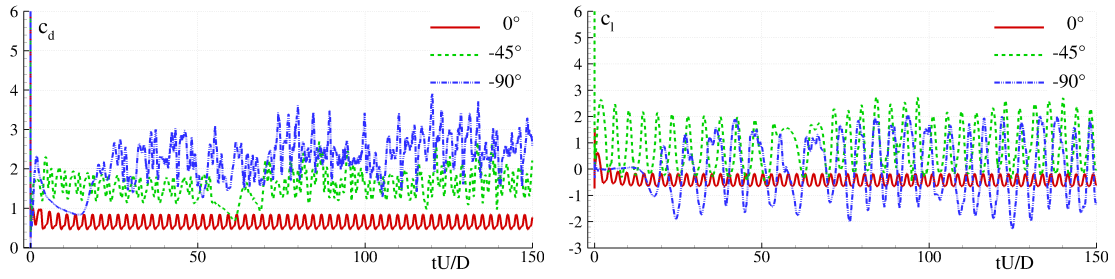
Table 3: Flow around a C-Shape body at Re=2000: main discretization parameters.

$D/\Delta r$	$\mathrm{Re}_{\Delta r}$	Co	$\Delta t_a U/D$	$\Delta t_d U/D$ (Dom 1)
200	10.0	1.76	8.81×10^{-3}	1.76×10^{-2}

For positive angles of attack (Figs. 13(a), 13(b)) the mean drag increases with α, however, for $\alpha=90°$ an almost periodic regime is reached again with a mean drag which is the highest recorded for all the five angles.

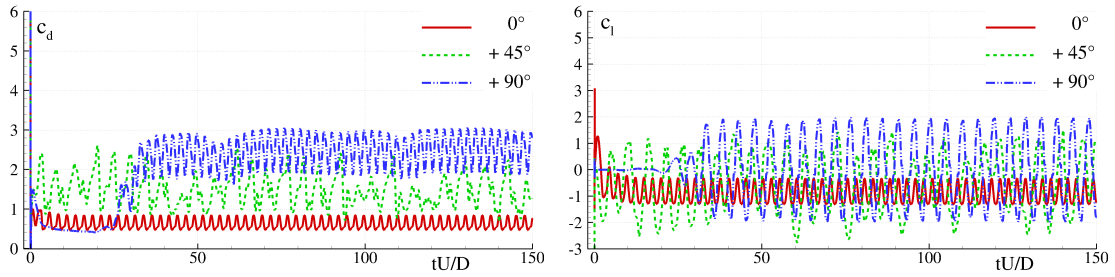
What is really non intuitive from the results presented is the negative mean value of the lift coefficient for $\alpha=0°$ and the high mean value of the drag coefficient for $\alpha=90°$. Analysing more deeply the case α=0°, from the pressure profile along the body contour it

https://doi.org/10.4208/cicp.271014.200415a Published online by Cambridge University Press



(a) (b)

Figure 12: Drag (a) and lift (b) coefficients for a C-shape body at Re=2000. Influence of the orientation: α=0°, −45°, −90°.



(a) (b)

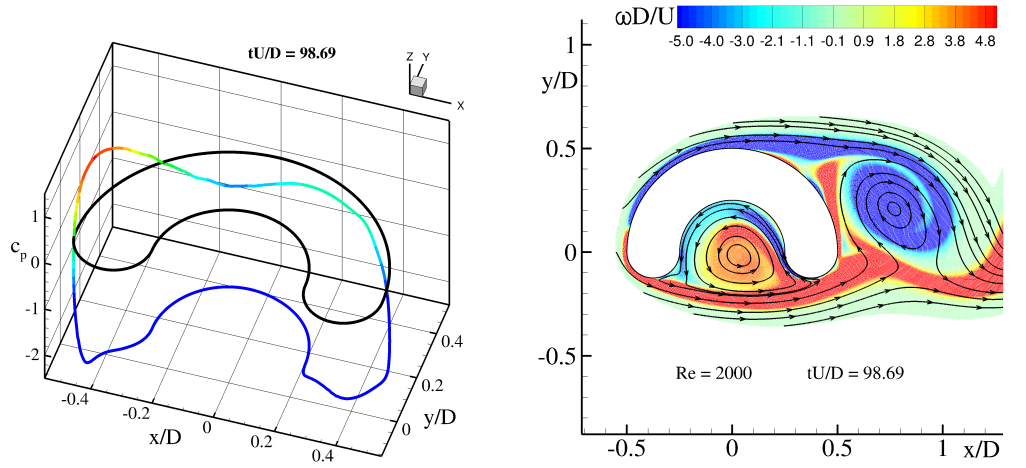
Figure 13: Drag (a) and lift (b) coefficients for a C-shape body at Re=2000. Influence of the orientation: α=0°, 45°, 90°.

is possible to see that (Fig. 14(a)) there is an higher pressure on the upper part of the body than in the lower part which is everywhere negative. This happens because a driven-cavity like flow establishes in the lower part of the body in which an almost steady vortex is entrapped by the flow itself (Fig. 14(b)). Conversely the flow in the upper part of the body behaves like the one generated by a circular cylinder inducing a quite regular vortex shedding (see Fig. 15).

For the case $\alpha = 90°$, in the initial stage of the wake development the vorticity field past the body is similar to that of a circular cylinder at the same Reynolds (see Figs. 16(a), 16(b) and 16(c)). Once the vortex shedding starts, at each cycle a vortex is entrapped inside the cavity in the body (see Figs. 16(d), 16(e) and 16(f)). This process induces a large flow dissipation which is responsible of the high drag developed in this condition.

Note that the total perimeter of the body is πD so that a comparison of the drag and lift coefficients with those for a circular cylinder with diameter D is possible for the case $\alpha = 0°$, 90° (the only one where an almost periodic behaviour is attained). From Fig. 17(a) the drag coefficient for the cylinder at Re= 2000 lays between that of the C-shape at the two different angles. The lift coefficient for the cylinder behaves similarly to the one of the C-shape with $\alpha = 90°$ (Fig. 17(b)).

https://doi.org/10.4208/cicp.271014.200415a Published online by Cambridge University Press



(a) (b)

Figure 14: C-shape at Re=2000, $\alpha=0°$ and $tU/D=98.69471$: (a) Pressure coefficient, the black line shows the c_p zero value. (b) Vorticity field and streamlines near body. Note the vortex trapped inside the cavity by the flux itself.

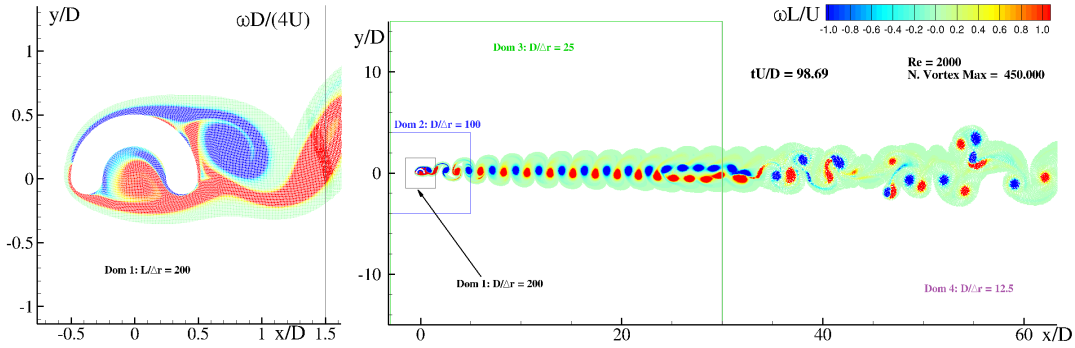


Figure 15: Flow around a C-Shape body at Re=2000 with $\alpha=0°$: evolution of the vorticity field past the body.

4.4 Flow around an impulsively started circular cylinder at Re=9500

As a further test-case, the simulation of the flow past a circular cylinder at Re=9500 is computed in order to compare with results presented in the literature [18]. The latter were published twenty years ago and at that time, due to the CPU resources available, the authors simulated only the semi-plane $y>0$ and stopped the simulation at time $tU/D=4.0$ (being D the cylinder diameter).

Fig. 18(a) shows the comparison with the DVH results for the drag coefficient.

Fig. 18(b) displays a longer time history for the drag coefficient. Indeed, nowadays, with a Vortex Particle method, using a Desktop PC with OpenMP parallel programming, it is possible to simulate long time evolution, $t_{end}U/D=100$, at this Reynolds recording

https://doi.org/10.4208/cicp.271014.200415a Published online by Cambridge University Press

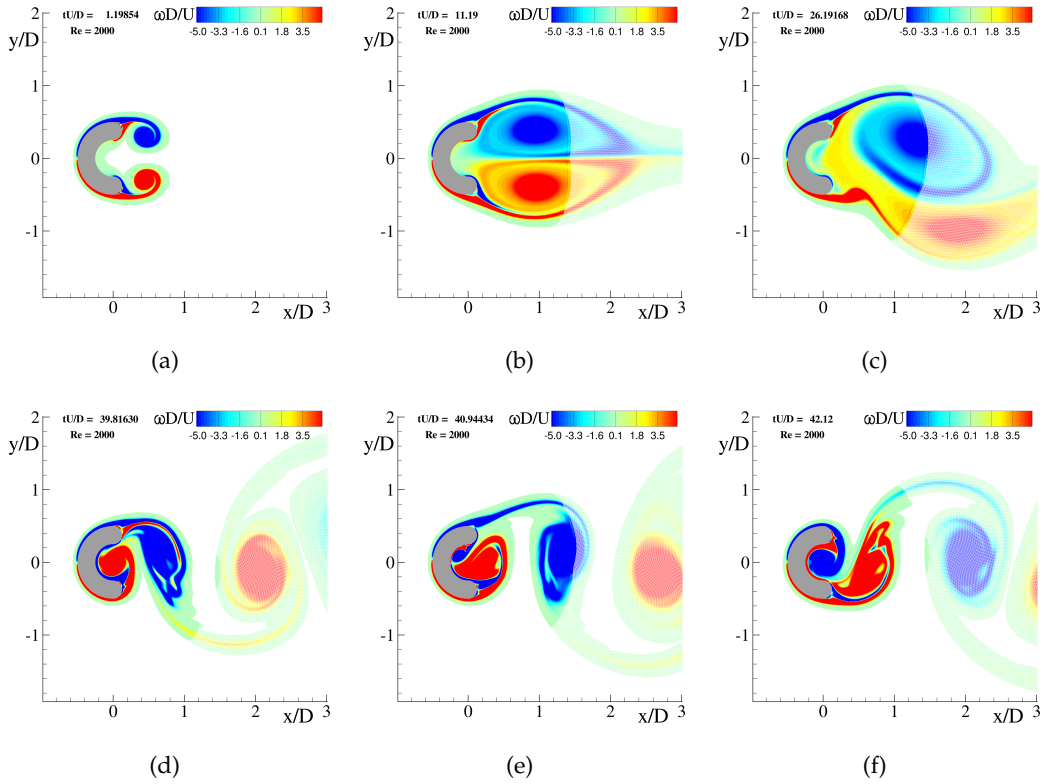


Figure 16: Flow around a C-Shape body at Re=2000 with α=90°: evolution of the vorticity field past the body.

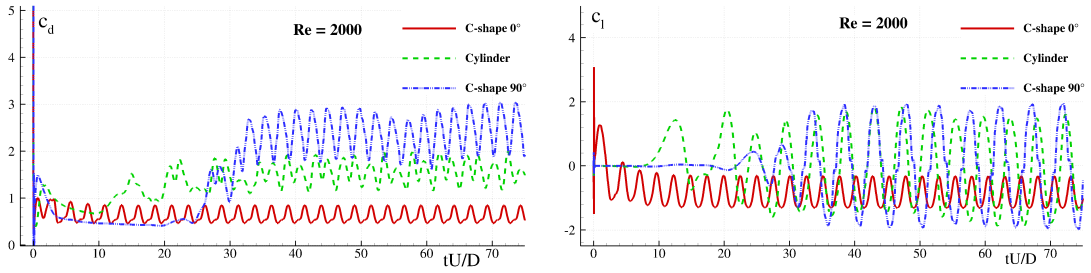


Figure 17: Flow around a C-Shape body at Re=2000 with α=0, 90°. Drag and lift coefficients are compared to that obtained with a circular cylinder at the same Re.

different wake oscillations and using a high spatial resolution close to the cylinder surface, $D/\Delta r$=800. This simulation remains quite critical to perform with a standard mesh-based solver, since the wake shape changes in time and it is not possible to build a-priori an optimum mesh for capturing all the vortical structures. Furthermore, the number of mesh-points involved would be very high because the irrotational region needs also to be

https://doi.org/10.4208/cicp.271014.200415a Published online by Cambridge University Press

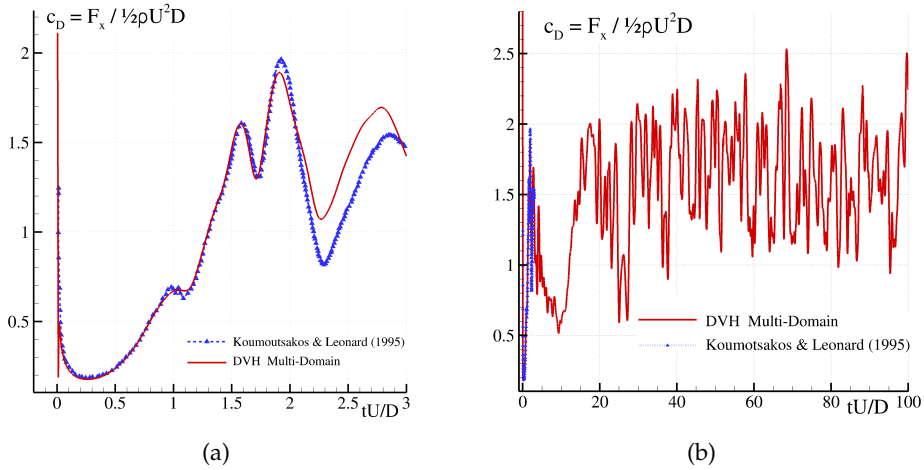


Figure 18: (a) Comparison of the drag coefficient between Koumoutsakos & Leonard (1995) [18] and DVH. (b) Time history of the drag coefficient for a longer time range.

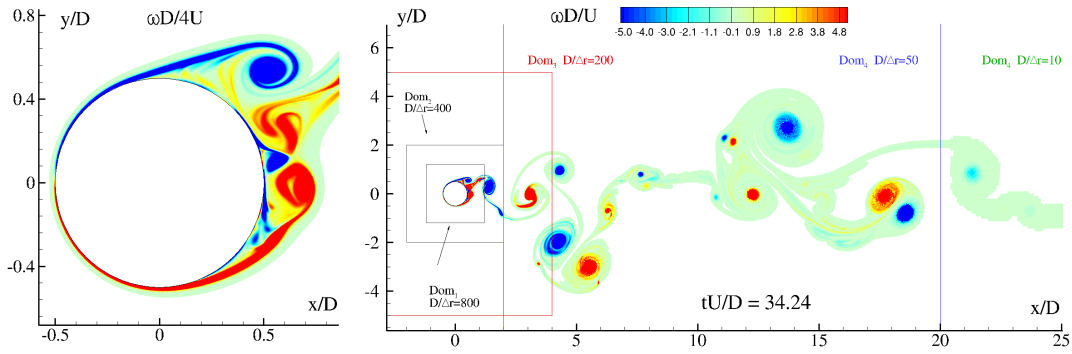


Figure 19: DVH vorticity field for the flow past an impulsively started circular cylinder at Re=9500.

solved. For this reason is quite unusual, even in a 2D framework, to find in the literature numerical results like the one here discussed.

Table 4 reports for the ratio $D/\Delta r$ used: (i) the cell-Reynolds number, (ii) the Courant number used for the advection steps, (iii) the ratio between the wall distance $y+=1$, measured at distance equal to the cylinder radius, R, from the stagnation point and Δr. This last parameter shows that the adopted resolution is able to well reproduce the boundary layer for the present Reynolds number.

Table 4: Flow around a Circular cylinder at Re=9500: main discretization parameters.

$D/\Delta r$	$\mathrm{Re}_{\Delta r}$	Co	$(y+=1)_R/\Delta r$	$\Delta t_a U/D$	$\Delta t_d U/D$ (Dom 1)
800	11.88	2.09	1.2	2.62×10^{-3}	5.23×10^{-3}

https://doi.org/10.4208/cicp.271014.200415a Published online by Cambridge University Press

Left plot of Fig. 19 shows the vorticity field close to the cylinder while the right plot displays the vorticity in the wake region also. One of the main features of the present model is the ability to simulate complex dynamics in the wake region. For example, in Fig. 20(a), after the build up of vorticity in the recirculation zone, the detachment of a first dipole composed of two large vortices of opposite signs can be appreciated. After a time interval of $tU/D=4$ another dipole, less intense with respect to the previous one, is detached from the cylinder (Fig. 20(b)). These first two dipoles interact in such a way that the second dipole "steals" the counter-clockwise rotating vortex from the first dipole (Figs. 20(c) and 20(d)) creating a new vortical structures which starts to orbit around the first clockwise shed vortex. After this interaction a third and a fourth dipole are detached from the cylinder; the first one travelling downwards towards the limit of the computational domain (Fig. 20(e)).

4.5 Flow past circular cylinder up to Re=100,000

The flow past an impulsively started cylinder at Re=50,000 and Re=100,000 is considered as a final test case. For these cases a very high spatial resolution is required in the boundary layer region. For this purpose eight RPDs are used, and close to the body the resolution $D/\Delta r$ is set equal to 3200. Table 5 reports the main discretization parameters used for four different Reynolds numbers 1000, 9500, 50,000, 100,000. For all the Reynolds numbers the ratio between the wall distance $y+=1$ (measured at distance equal to the cylinder radius, R from the stagnation point) and Δr, is maintained of order of one to guarantee to have enough vortex particles even in the viscous sublayer region ($y+<5$).

Table 5: Flow around a circular cylinder at different Reynolds numbers: main discretization parameters.

Re	$D/\Delta r$	$\mathrm{Re}_{\Delta r}$	Co	$(y+=1)_R/\Delta r$	$\Delta t_a U/D$	$\Delta t_d U/D$ (Dom 1)
1000	200	5	1.74	1.6	8.69×10^{-3}	8.69×10^{-3}
9500	800	3.75	1.32	2.8	2.62×10^{-3}	5.23×10^{-3}
5×10^4	3200	15.63	1.84	1.4	5.74×10^{-4}	1.72×10^{-3}
10^5	3200	31.25	1.84	0.8	5.74×10^{-4}	3.44×10^{-3}

Fig. 21 depicts the vorticity field past an impulsively started circular cylinder at Re=100,000 for four time instants. Around time $tU/D=0.50$ the boundary layer in the rear part of the cylinder starts to destabilize and vortical dipole structures are released in the wake region. This kind of phenomenon clearly shows the complexity of the flow field at this Reynolds number. In order to highlight the complexity of the wake for such high Reynolds numbers, the vorticity fields have been reported in Fig. 22 at four different Reynolds numbers. For the two highest Reynolds numbers the symmetry of the numerical solution is already lost at tU/D=4.0. Indeed, due to the complex vorticity interactions, the small asymmetries in the RDP, generated by the packed algorithm, are large enough to induce this behaviour. In Fig. 23 the drag coefficients for the four Reynolds numbers, 1000, 9500, 50,000, 100,000 are reported. This results shows that a drag-crisis appears

https://doi.org/10.4208/cicp.271014.200415a Published online by Cambridge University Press

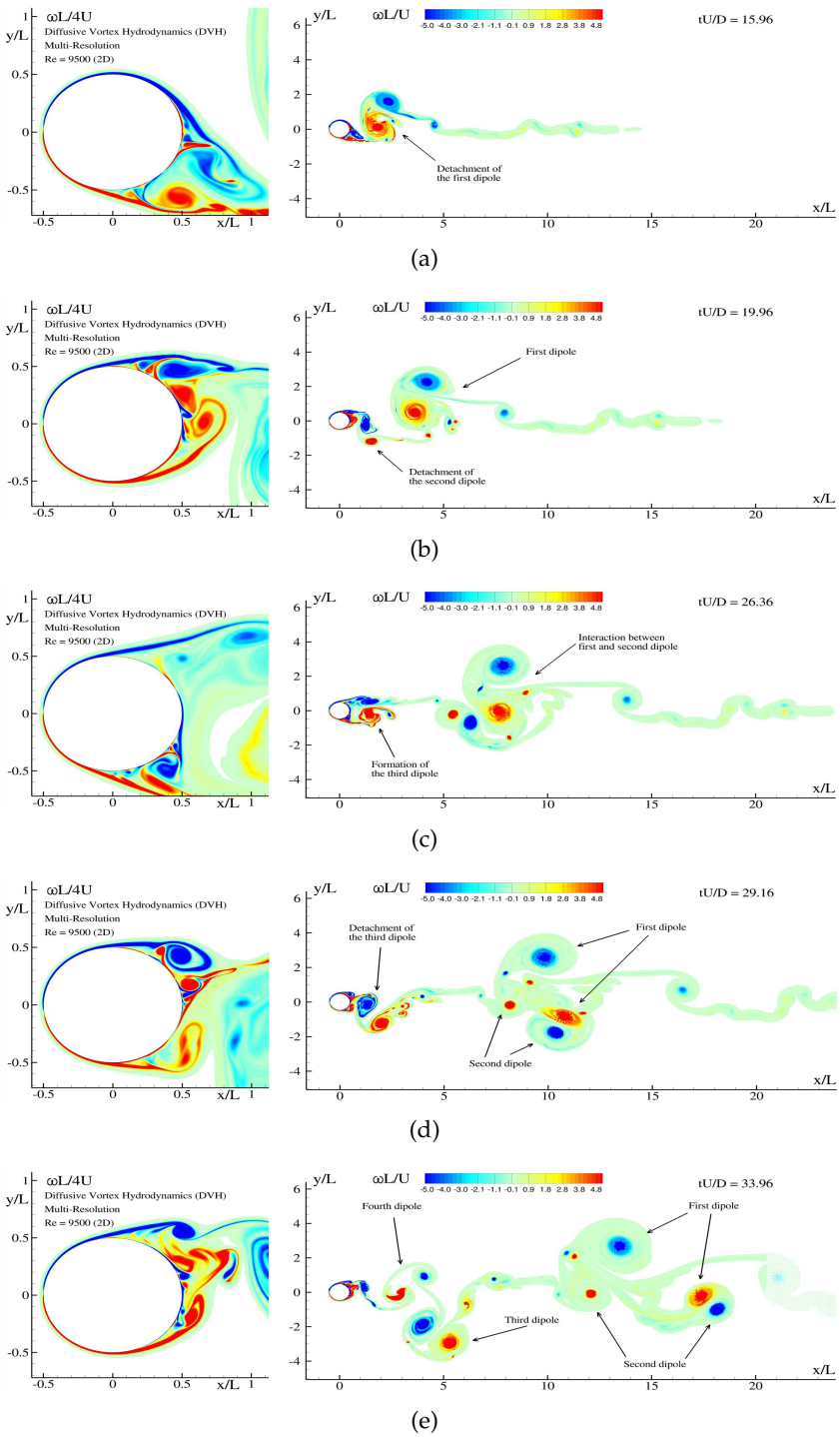


Figure 20: Wake past an impulsively started cylinder at Re 9500: flow development for increasing times.

https://doi.org/10.4208/cicp.271014.200415a Published online by Cambridge University Press

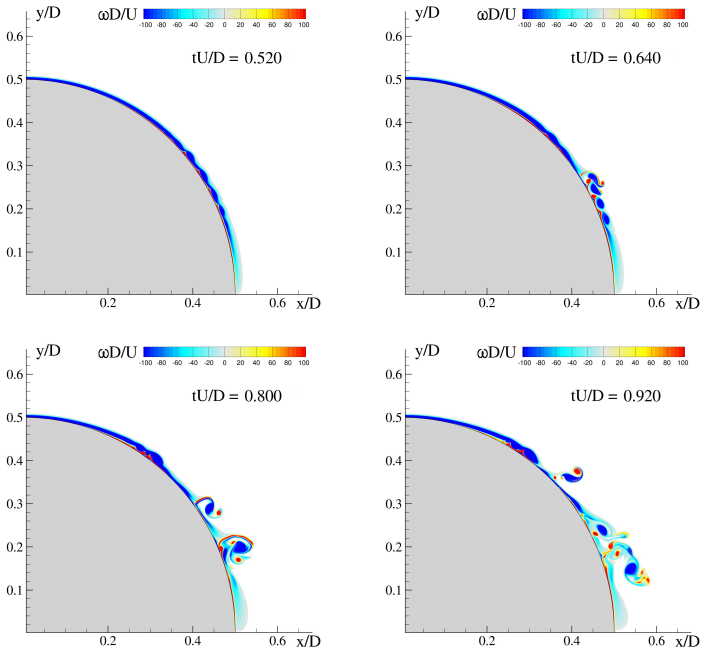


Figure 21: Flow around an impulsively started circular cylinder at Re= 100,000. Vorticity field for four times tU/D=0.52, 0.64, 0.80, 0.92.

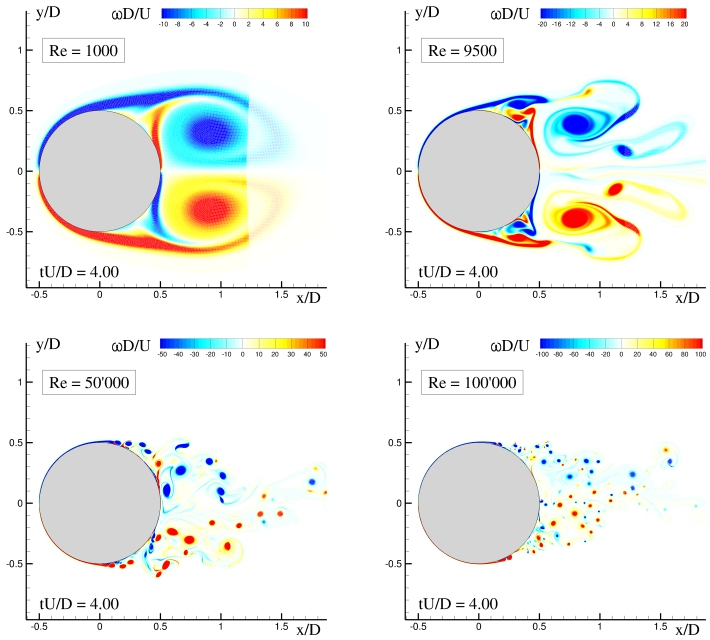


Figure 22: Flow around an impulsively started circular cylinder at four different Reynolds numbers. Vorticity field at the same non dimensional time tU/D=4.

https://doi.org/10.4208/cicp.271014.200415a Published online by Cambridge University Press

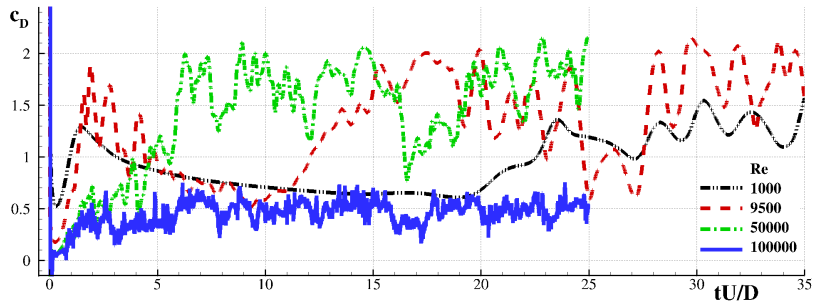


Figure 23: Flow around an impulsively started circular cylinders at four different Reynolds numbers. Drag coefficient time histories for Reynolds numbers: 1000, 9500, 5×10^4 and 10^5.

between Re=50,000 and 100,000 and this is also confirmed in by [26] for a 2D-framework. We were not able to find in the literature numerical solutions at the two highest Reynolds numbers presented here (without using any turbulence models). Therefore, we think that the presented results can be useful also for other readers who need to test numerical solvers at these viscosity levels.

5 Computational resources

All the simulations presented in this work have been performed on Desktop PC with six cores Xeon(R) CPU X5650, 2.3GHz, using a simple OpenMP parallel programming. The CPU cost of the implemented code is about 100μs per vortex particle and per time iteration on a single core. The max number of used particle is of order 10^6 and the allocated memory did not exceed 1 Gbyte. Table 6 displays, for some test-case studied in this work, the total CPU cost and the main parameters adopted.

Table 6: DVH solvers CPU time costs for simulating the flow past elliptic and circular cylinders at various Reynolds number. Here L is a characteristic length of the problem and can be taken as the chord for the ellipse and as the diameter for the cylinder.

	Ellipse Re=3000	Cylinder Re=9500	Cylinder Re=50,000	Cylinder Re=100,000
$L/\Delta r$ (Dom 1)	800	800	3200	3200
$R_d/\Delta r$	4	4	4	4
N vortices	1,100,000	1,400,000	1,900,000	1,700,000
N iterations	30,259	38,222	43,573	43,573
$t_{end}U/L$	50	100	25	25
$\Delta t_a U/L$	$1.65\,10^{-3}$	$2.62\,10^{-3}$	$5.74\,10^{-5}$	$5.74\,10^{-5}$
CPU time (6 cores)	7.5 days	10 days	16 days	15 days

https://doi.org/10.4208/cicp.271014.200415a Published online by Cambridge University Press

6 Conclusions

In this work a new Particle Vortex Method, called Diffused Vortex Hydrodynamics (DVH), has been presented. The numerical method has been used to simulate viscous incompressible flows.

The DVH is based on the splitting algorithm of Chorin (1973) [4] for which the time integration is divided in diffusion and advection time steps. Regarding the latter, the velocity field is obtained using a convolution sum among the circulations carried by the vortex particles and the particles are then advected with this velocity field. For what concerns the diffusion step, each vortex particle gives a vorticity contributions on "Regular Point Distributions" (RPD) through the elementary solution of the heat equation. This procedure prevents the excessive clustering or rarefaction of the vortex particles and substitutes remeshing procedures usually adopted in this kind of method. The RPD is a special set of points where the new vortex particles at the end of each diffusion step are generated. Close to the solid bodies RPDs are generated through a packing algorithm [7] which is embedded in the solver thanks to the fact that it is also based on a particle interaction dynamics. The packing algorithm collocates points regularly around body of arbitrary shape allowing for the enforcement of no-slip boundary condition exactly on the solid surfaces. Far from the solid surfaces simple Cartesian lattice can be used. All the different RPDs can overlap each other and can be characterized by different spatial resolutions. With the DVH model different spatial resolutions can be handled in an easy way without the necessity to use complex procedures for the matching of the solution among the different domains used.

The presence of a solid body within the flow domain results in the introduction of a suitable procedure both to generate vorticity on its surface and to enforce the impermeability constraint. Indeed, the velocity field is decomposed in: (i) a free stream contribution, (ii) the velocity induced by the vortex particles and (iii) the contribution to the velocity field due to the presence of a body. The latter is evaluated through a potential field using an indirect formulation in complex variables [14]. From all the contributions it is possible to generate the new set of vortices on the body surface enforcing the no-slip condition exactly.

The present method is tested and validated on different problems of increasing complexities up to flows with Reynolds number equal to 100,000 (without using any turbulence model).

For future developments, body surface with singularities will be treated. The method will be extended for solving problems with multiple bodies which can move and/or deform. Finally, the extension to 3D is under construction.

Acknowledgments

This paper is dedicated to the memory of Maurizio Landrini. Many parts of the presented research activity have been inspired by his works on Poincaré and integral repre-

https://doi.org/10.4208/cicp.271014.200415a Published online by Cambridge University Press

sentations of the velocity field. The research leading to these results has received funding by the Flagship Project RITMARE – The Italian Research for the Sea – coordinated by the Italian National Research Council and funded by the Italian Ministry of Education, University and Research within the National Research Program 2014-2015.

References

[1] L.A. Barba, A. Leonard, and C.B. Allen. Advances in viscous vortex methods-meshless spatial adaption based on radial basis function interpolation. *International Journal for Numerical Methods in Fluids*, 47(5):387–421, 2005.

[2] L.A. Barba, A. Leonard, and C.B. Allen. Numerical investigations on the accuracy of the vortex method with and without remeshing. In *16th AIAA Computational Fluid Dynamics Conference*, June 2003.

[3] M.G. Benson, P.G. Bellamy-Knights, J.H. Gerrard, and I. Gladwell. A viscous splitting algorithm applied to low reynolds number flows round a circular cylinder. *Journal of Fluids and Structures*, 3(5):439–479, 1989.

[4] A. Chorin. Numerical study of slightly viscous flow. *Journal of Fluid Mechanics*, 57(04):785–796, 1973.

[5] A. Chorin. Vortex sheet approximation of boundary layers. *Journal of Computational Physics*, 27(3):428–442, 1978.

[6] I.P. Christiansen. Numerical simulation of hydrodynamics by the method of point vortices. *Journal of Computational Physics*, 13(3):363–379, 1973.

[7] A. Colagrossi, B. Bouscasse, M. Antuono, and S. Marrone. Particle packing algorithm for SPH schemes. *Computer Physics Communications*, 183(2):1641–1683, 2012.

[8] A. Colagrossi, G. Graziani, and M. Pulvirenti. Particles for fluids: SPH vs vortex methods. *Journal of Mathematics and Mechanics of Complex Systems*, 2(1):45–70, 2014.

[9] G.-H. Cottet and P.D. Koumoutsakos. *Vortex Methods: Theory and Practice*. Cambridge University Press, University Printing House, Shaftesbury Road, Cambridge, United Kingdom, 2008.

[10] M. Coutanceau and R. Bouard. Experimental determination of the main features of the viscous flow in the wake of a circular cylinder in uniform translation. Part 1. Steady flow. *Journal of Fluid Mechanics*, 79(02):231–256, 1977.

[11] E. Edwards and R. Bridson. A high-order accurate particle-in-cell method. *International Journal for Numerical Methods in Engineering*, 90(9):1073–1088, 2012.

[12] J.D. Eldredge. Efficient tools for the simulation of flapping wing flows. *AIAA*, 85(2005):1–11, 2005.

[13] G. Graziani and P. Bassanini. Unsteady viscous flows about bodies: Vorticity release and forces. *Meccanica*, 37(3):283–303, 2002.

[14] G. Graziani and M. Landrini. Application of multipoles expansion technique to two-dimensional nonlinear free-surface flows. *Journal of Ship Research*, 43(1):1–12, 1999.

[15] G. Graziani, M. Ranucci, and R. Piva. From a boundary integral formulation to a vortex method for viscous flows. *Computational Mechanics*, 15(4):301–314, 1995.

[16] R.W. Hockney and J.W. Eastwood. *Computer Simulation Using Particles*. Adam Hilger, Bristol, 1988.

[17] C.-J. Huang and M.-J. Huang. A vortex method suitable for long time simulations of flow over body of arbitrary geometry. *Computers & Fluids*, 74:1–12, 2013.

https://doi.org/10.4208/cicp.271014.200415a Published online by Cambridge University Press

[18] P. Koumoutsakos and A. Leonard. High-resolution simulations of the flow around an impulsively started cylinder using vortex methods. *Journal of Fluid Mechanics*, 296:1–38, 1995.
[19] F. Macià, M. Antuono, L.M. González, and A. Colagrossi. Theoretical analysis of the no-slip boundary condition enforcement in SPH methods. *Progress of Theoretical Physics*, 125(6):1091–1121, 2011.
[20] S. Marrone, B. Bouscasse, A. Colagrossi, and M. Antuono. Study of ship wave breaking patterns using 3D parallel SPH simulations. *Computers & Fluids*, 69(0):54–66, 2012.
[21] S. Marrone, A. Colagrossi, M. Antuono, G. Colicchio, and G. Graziani. An accurate SPH modeling of viscous flows around bodies at low and moderate reynolds numbers. *Journal of Computational Physics*, 245(0):456–475, 2013.
[22] M.T. Nair and T.K. Sengupta. Unsteady flow past elliptic cylinders. *Journal of Fluids and Structures*, 11(6):555–595, 1997.
[23] G. Riccardi and D. Durante. *Elementi di Fluidodinamica*. Springer, 2006.
[24] E. Rossi, A. Colagrossi, and G. Graziani. Numerical simulation of 2D-vorticity dynamics using particle methods. *Computers & Mathematics with Applications*, 69(12):1484-1503, 2015.
[25] M.S. Shadloo, A.Zainali, M.Yildiz, and A.Suleman. A robust weakly compressible SPH method and its comparison with an incompressible SPH. *International Journal for Numerical Methods in Engineering*, 89(8):939–956, 2012.
[26] S.P. Singh and S. Mittal. Flow past a cylinder: Shear layer instability and drag crisis. *International Journal for Numerical Methods in Fluids*, 47(1):75–98, 2005.
[27] L. Van Dommelen and E.A. Rundensteiner. Fast, adaptive summation of point forces in the two-dimensional poisson equation. *Journal of Computational Physics*, 83(1):126–147, 1989.

https://doi.org/10.4208/cicp.271014.200415a Published online by Cambridge University Press